Experimental and Numerical Investigation of the Drying of an Agricultural Soil

Njaka Ralaizafisoloarivony[1], *Kien* Tran[1,2], *Aurore* Degré[1], *Benoît* Mercatoris[1], *Angélique* Léonard[3], *Dominique* Toye[3], and *Robert* Charlier[2,*]

[1]University of Liège, Gembloux Agro-Bio Tech, 5030 Gembloux, Belgium
[2]University of Liège, Department ArGEnCo, Quartier POLYTECH 1, 4000 Liège, Belgium
[3]University of Liège, Chemical Engineering, 4000 Liège, Belgium

Abstract. Due to climate change, soil desiccating became a serious concern in the agricultural area of Belgium. Knowing soil evaporation kinetic can help to elucidate and predict: the soil moisture regime, soil water retention and soil water content. Those parameters are vital for water use efficiency and sustainable agriculture. This research analysed the mechanism of soil evaporation both under laboratory experiment and numerical modelling. Soil samples (Luvisol) were collected from the agricultural field in Gembloux-Belgium, and processed in a small drying chamber. Sensors measured the chamber temperature and humidity, while digital camera monitored the soil surface throughout the experiment. HYPROP device recorded the water change, soil suction, and soil water retention curve. During three evaporation experiments, four periods were observed rather than three according to the common theory. The modelling considered thermo-hydro-mechanical framework for predicting the drying process of Luvisol. The model used the finite element code LAGAMINE created at the University of Liege. The Software aims at assessing the mechanism of water transport between soil and atmosphere. The results of the simulation showed major domination of Darcean flow during desiccating, while some short vapour diffusion occurred only after the soil surface began to de-saturate.

1 Introduction

The process of evaporation is quite complicated in agricultural soil since it is conditioned by the soil characteristics (textures, structure, etc.), soil management (tillage, covered crop, etc.), and the environmental condition (precipitation, temperature, etc.). The increase of the world temperatures raised the soil evaporation rate, leading to severe crop water stress and considerable yield loss. In Belgium, several dry spells (no rainfall) were recorded over the course of the 21st century [1]. Understanding the kinetic of evaporation of the Luvisol (soil of Belgium) will help to find appropriate method to enhance water use efficiency and alleviate the effect of climate change on plant water stress. This study demarcated from previous study since it utilized very accurate device and coupled it with hydro-thermo-mechanical model prediction.

Based on previous studies, three distinct periods of evaporation occurred during the process of drying [2]. The first period is a Constant Rate Period (CRP) during which the evaporation rate is at its highest and constant. When the soil water supply decreases, there is prompt drop of the soil evaporation called “critical-moisture content”, indicating the start of the first Falling Rate Period (FRP 1) [3, 4]. The soil surface starts to dry drastically till the third period called second Falling Rate Period (FRP 2). The evaporation is very low due to strong interacting forces at the soil liquid-solid interface. Despite wide knowledge of the process, it is not well understood if the soil water evaporation is mainly due to liquid transport by capillary or by gas diffusion transport. Moreover, the soil characteristics and its behaviour will play huge roles in this mechanism [5, 6].

In general, there is a complex soil hydro-thermo-mechanical behaviour. Any change in soil temperature, shrinkage, porosity, etc. affects the soil water evaporation. Those in turn impact the water suction, water content, contaminant transport, available water for plant etc. [7, 8]. Previous numerical estimation model assessed the drying mechanism at pore level (ex: Pore network Model). They were limited to isothermal condition and non-deformable sample due to the need for high speed computer [9]. Continuum models were commonly used for evaporation test [10,11]. Gerard et al. [12] coupled hydro-thermal conditions to simulate convective drying of a silt soil. Prime et al. [13] and An et al. [14] used the same method for limestone and sand, respectively. It was Hubert et al. [15] who added the mechanical parameter to monitor the drying process of pure clay. This study used agricultural soil and considered water flow (hydro-), temperature (thermo-) and soil shrinkage (mechanical) to model the kinetic of evaporation.

* Corresponding author: Robert.Charlier@uliege.be

2 Materials and Methods

2.1 Sampling

Three composite soils were sampled from 0-10cm depth from an agricultural site in Gembloux-Belgium. The soil was a Cutanic Luvisol based on WRB (World Reference Base soil classification) and contained about 70% silt, 20% clay and 10% sand. The bulk density was measured after oven drying the samples from rings at 105°C during 24h. Another oven dried sample (at 40°C for one week) was crushed, sieved at 2mm sieve, and compressed on three core rings (5cm height x 8cm diameter) to form the original bulk density. Those three samples were used during the study.

2.2 Device preparation and analysis

Drying experiment was conducted in a chamber dryer using HYPROP device (UMS GmbH, Munich, Germany). The device is very accurate for continuous measurement of water evaporation, water suction (from 0-100kPa) and water retention.

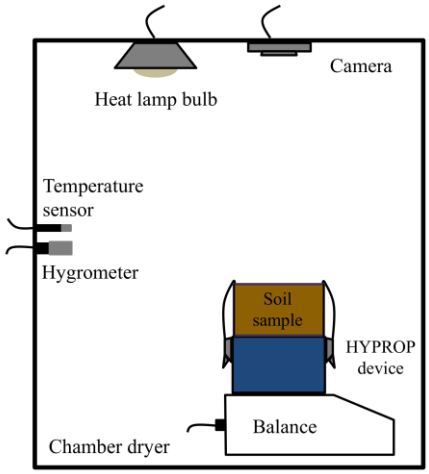

Fig. 1. Drying chamber of the experiment

The samples were saturated for 24h and inserted on the HYPROP package. The soil surface was exposed to a free evaporation. Precision balance (0.01g) monitored the soil weight. Temperature and relative humidity were measured with Platinum resistance thermometer (PT1000) and DHT22 sensors (2-5% accuracy). A canon digital camera (12 Mpixel), placed 0.5m above the sample, monitored the soil shrinkage. All data was recorded every one min except for the camera (30 min).

The HYPROP package came with hydraulic models to fit the data including: Mualem, Van Genuchten, Durner models, etc. For the evaporation prediction, the model used was the LAGAMINE code [16] with Finite Element Method. It predicted the process of moisture transfer between the soil surface and the ambient.

3. Experimental results

The evaporation rate was observed through the water loss per surface unit and per time:

$$\bar{q} = -\frac{1}{A}\frac{dm}{dt} \qquad (1)$$

Where: m[kg] and A[m2] were the mass and sample surface, respectively. Figure 2 showed the soil evaporation per time. All Three tests presented high fluctuation in the beginning, but depicted rather similar trend for the rest of the experiment.

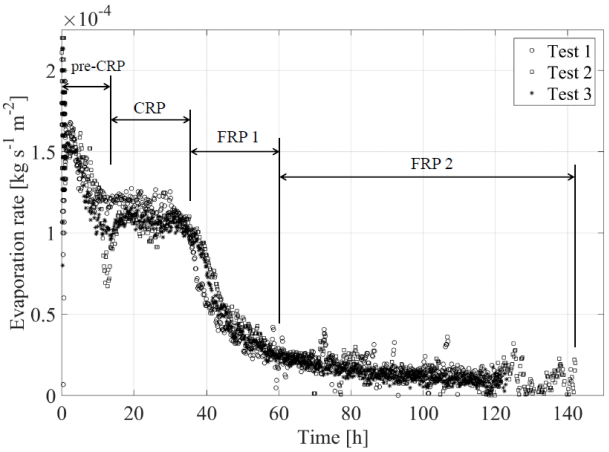

Fig. 2. Change of evaporation rate with time

Four distinct periods of evaporation were observed instead of three as the classical concept. Figure 2 presented a pre-CRP period during the first 15h which was characterised by high evaporation rate attaining 1.2 x 10^{-4} kg $s^{-1}m^{-2}$. This was due to the excess of water in the beginning and the pre-heating of the chamber. The second period CRP occurred when the evaporation attained around 10^{-4} kg $s^{-1}m^{-2}$. The CRP lasted for about 20h, passed through a “critical-moisture content", then continued to the third period (FRP1) when the evaporation rate declined. The sample surface experienced a rapid drying. The beginning of the last period FRP2 was observed as soon as the evaporation rate arrived at its lowest. Cracks of 3cm length and 0.2 cm wide were observed above the tensiometer, but they had no major effect on evaporation.

3.2 Soil temperature evolution

Figures 3 showed the temperature above and below the samples (illustration of test 3). During the pre-CRP, the bottom and the surface temperatures increased at the same rate. Temperatures were almost constant throughout the CRP periods. Since the evaporation rate was constant, the result indicated that the applied heat was compensated proportionately by the produced vapour. When there is not enough water vapour during FRP, the soil temperature raised to reach the ambient temperature. Similar result was found by Kowalski [17]. He observed that the stagnant temperature during CRP was the wet-bulb temperature *Th* which can be calculated from the relation proposed by Stull [18]. Based on it, the calculated wet-bulb temperatures of our samples were 19.1, 19.7 and 21.3°C, respectively. The difference in values was due to the difference of the temperature during the experiment.

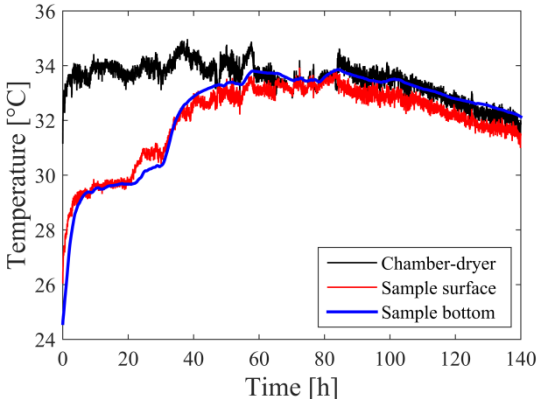

Fig. 3. Soil temperature evolution with time (test 3)

3.3 Shrinkage

The shrinkage was observed from sequenced images taken from fixed camera. ImageJ software converted the coloured image into gray 8-bit and in binary images. The change in pixel value from one image to another indicated the shrinkage (Figure 4). The shrinkage in percentage indicated the ratio between the shrinkage areas over the total area of sample surface. The soil surfaces were reduced by 6.7%, 5.1%, and 6.2%, for the three samples. The shrinkage took place during the pre-CRP. Most of the 65%-75% of the surface shrinkage occurred above a degree of saturation of 0.75.

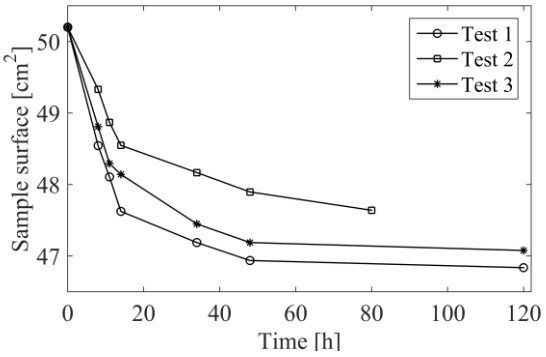

Fig. 4. Soil surface shrinkage with time

4 Couple thermo-hydro-mechanical model

4.1 Mechanical model

Soil mechanical properties (i.e. stiffness or modulus) were related to soil moisture content [19, 20, 21]. The results showed an increase of soil modulus with matric suction due to volumetric shrinkage. The relationship shrinkage vs. degree of saturation was not linear; therefore, we choose a nonlinear mechanical model in the study relating soil stress and strain. The work on Bishop's effective stress was used as it is related to soil suction. The strain is related to stress, and the moduli in the equation are not constants. In order to reproduce the nonlinear behaviour of the soil, equation 5 was replaced by equation 7 which evolved with the suction p_c.

$$\sigma'_{ij} = \sigma_{ij} - p_g\delta_{ij} + S_r(p_g - p_w)\delta_{ij} \quad (2)$$

(Where: σ'_{ij} effective stress tensor, σ_{ij} total stress tensor, Sr water saturation, δ_{ij} Kronecker's tensor, p_g and p_w gas and water pressure)

$$\sigma'_{ij} = D^e_{ijkl}\varepsilon_{ij} \quad (3)$$

$$D^e_{ijkl} = 2G\delta_{ik}\delta_{jl} + (K - \tfrac{2}{3}G)\delta_{ij}\delta_{kl} \quad (4)$$

$$K = \frac{1+e}{3k}\sigma'_m \quad (5)$$

$$G = \frac{3(1-2\nu)}{2(1+\nu)}K \quad (6)$$

$$K = \frac{K_0}{3(1-2\nu)}\{(k_1 - 1)[1 - exp(-k_2 p_c)] + 1\} \quad (7)$$

Where: σ'_{ij} elastic stress tensor, D^e_{ijkl} global elastic tensor, ε_{ij} elastic strain, K and G bulk and shear moduli, k slope of the unloading-reloading, e void ratio, ν Poisson's ratio of the porous medium, K_0 initial value of the bulk modulus, k_1 and k_1 model parameters.

4.2 Hydraulic model

The fluid transport was predicted by a biphasic flow model in porous media. The advective fluxes of liquid and gas were determined by Darcy's law. We assumed that the media were non-reactive material, so that water and gas flow depended on the degree of saturation only. This last was defined by the water storage and the capillary pressure, and calculated by the dual porosity model of Durner [22]. The water retention was measured by Mualem [23] model and the diffusive flux by Fick's law.

$$q_w = -\frac{k_w}{\mu_w}(\nabla p_w + \rho_w g) \quad (8)$$

$$q_g = -\frac{k_g}{\mu_g}(\nabla p_g + \rho_g g) \quad (9)$$

$$S_r = S_{res} + (S_{sat} - S_{res})\{w_1 \underbrace{[1 + (\alpha_1 p_c)^{-n_1}]^{m_1}}_{S_{e1}} + w_2 \underbrace{[1 + (\alpha_2 p_c)^{-n_2}]^{m_2}}_{S_{e2}}\} \quad (10)$$

Where: q_w and q_g mass fluxes of liquid and gas, k_w and k_g water and gas permeability, μ_w and μ_g dynamic viscosities water and gas, p_w and p_g water and gas pressure, S_r degree of saturation, p_c capillary pressure, i pores structures, w_i weighing factors, α_1 inverse of air entry pressure, S_{sat} and S_{res} water maximal saturation and the water residual saturation, m_i and n_i model parameters, $m_i = 1/n_i$.

$$k_w = K_w \frac{(w_1 S_{e1} + w_2 S_{e2})^l \{w_1 \alpha_1 \left[1 - \left(1 - S_{e1}^{\frac{1}{m_1}}\right)^{m_1}\right] +}{(w_1\alpha_1 + w_2\alpha_2)^2}$$

$$\frac{w_2\alpha_2\left[1-\left(1-S_{e2}^{\frac{1}{m_2}}\right)^{m_2}\right]^2}{(w_1\alpha_1+w_2\alpha_2)^2} \quad (11)$$

$$i_v = -D_{v\tau\emptyset}\,(1-S_r)\nabla_{\rho v} \quad (12)$$

$$RH = \frac{\rho_v}{\rho_{v,sat}} = exp\left(\frac{-p_c M_v}{\rho_w RT}\right) \quad (13)$$

$$\rho_{v,sat} = \{1994.4\,exp[-0.06374(T-273) + 0.1634\,x\,10^{-3}\,(T-273)^2]\}^{-1} \quad (14)$$

Where: k_w water retention, K_w saturated water permeability, l pore connectivity, i_v diffusive flux by Fick's law, D_v diffusion coefficient of vapour into dry air, τ and $\emptyset$ tortuosity and porosity, $\rho_v$vapour density, RH relative humidity, M_v molecular mass of the water vapour, R gas constant, T temperature in Kelvin, $\rho_{v,sat}$ saturated vapour concentration.

4.3 Heat transfer

The heat transfer in porous media is governed by the heat conduction following Fourier's law, the convective heat transfer for liquid, air and water vapour, and an additional heat flux related to the vapour flow.

$$V_T = -\Gamma_m\nabla T + \underbrace{[c_{p,w}\rho_w q_w + c_{p,a}\rho_a q_g + c_{p,w}(\rho_a q_g + i_v)](T-T_0)}_{convection} + \underbrace{(\rho_v q_g + i_v)L}_{latent} \quad (15)$$

(Where: $c_{p,w}$/$c_{p,a}$/ $c_{p,v}$ water/air/vapour specific heats, T_0 initial temperature, L water evaporation latent heat)

4.4 Thermo-hydraulic boundary condition

The boundary considered the transfer between the thin layers of soil surface and the ambient. The vapour flow and the heat transfer were due to vapour density difference and temperature difference between the ambient and the soil surface [24]. The radiant flux from the lamp-bulb and the air to the soil surface was estimated by the Stefan-Boltzmann equation.

$$\bar{q} = \alpha(\rho_{v,surf} - \rho_{v,air}) \quad (16)$$

$$\bar{f} = L\bar{q} - \beta\left(T_{air} - T_{surf}\right) - R_n \quad (17)$$

$$R_n = \varepsilon_s\sigma A\left(T_{air}^4 - T_{surf}^4\right) + R_{lamp} \quad (18)$$

Where: $\bar{q}$ vapour flow, α mass transfer coefficient, a driving potential, $\rho_{v,surf}$ and $\rho_{v,air}$ vapour density soil surface and ambient, $\bar{f}$ heat flux, β coefficient, T_{air} and T_{surf} temperature of soil surface and ambiant, R_n net radiant from Stefan-Botlzmann law, ε_s soil and bulb emissivity, σ constant of Stefan-Boltzmann, R_{lamp} flux term of lamp-bulb.

5. Numerical results and analysis

5.1 Geometric configuration of the simulation

The simulation was performed on 2D-axisymetric cylindrical soil subdivided in 20 x 50 mesh elements and with the boundary condition as described before (Figure 5). The sample was saturated and only the upper soil surface allowed water to pass. Table 1, 2, 3 and 4 present all hydraulic, thermal, and mechanicals parameters used in the models. Hydraulic parameters were extracted from HYPROP results. The predictive model was compared to the results from test 3 (Figure 6 to 11).

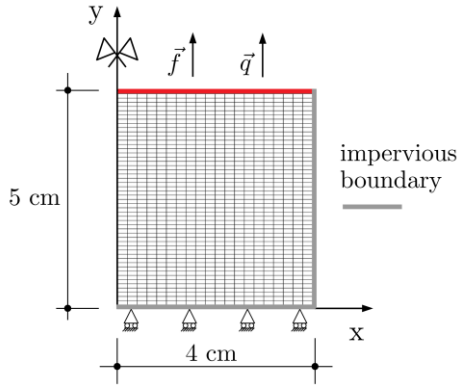

Fig. 5. Boundary condition of the model

Table 1. Mass and heat transfer coefficients

	α[ms^{-1}]	β[Wm^{-2}K^{-1}]
Test 1	0.0055	122.6
Test 2	0.0050	78.6
Test 3	0.0048	84.8

Table 2. Mass and heat transfer coefficients.

ρ_w[kgm^{-3}]	Liquid water density	1000
μ_w[Pas]	Water dynamic viscosity	1.E-3
K_w[m^2]	Water permeability	1.8E-12
α_1[cm^{-1}]	Inverse of air entry pressure (macro-pores)	0.1
α_2[cm^{-1}]	Inverse of air entry pressure (macro-pores)	0.025
m_1[-]	Durner model parameter	0.23
m_2[-]	Durner model parameter	0.41
S_{res}[-]	Residual water saturation	0

Table 3. Parameters of the thermal model

$c_{p,w}$[Jkg^{-1}K^{-1}]	Liquid water specific heat	4180
$c_{p,v}$[Jkg^{-1}K^{-1}]	Water vapour specific heat	1800

$c_{p,\alpha}$[Jkg^{-1}K^{-1}]	Air specific heat	1000
Γ_m[Wm^{-1}K^{-1}]	Medium thermal conductivity	0.9
L[Jkg^{-1}]	Water evaporation latent heat	2500

Table 4. Parameters of the mechanical model

ρ_s[kgm^{-3}]	Solid density	2650
∅[-]	Porosity	0.52
K_0[Pa]	Bulk modulus	1.E5
G_0[Pa]	Shear modulus	0.4E5
ν[-]	Poisson's ratio	0.25

5.2 Soil shrinkage

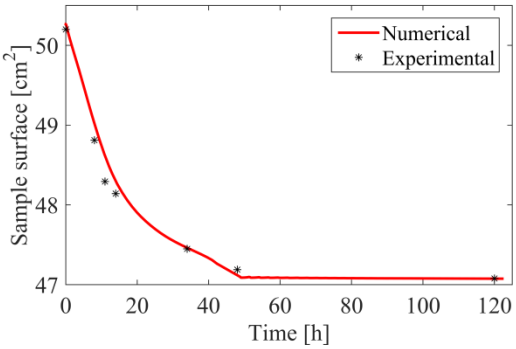

Fig. 6. Experimental and numerical surface shrinkage

The non-linear elasticity law allowed predicting the soil stiffness and gives good agreement with the result (Figure 6). The soil bulk modulus changed exponentially with the suction with k_1 = 1.2 10^4 and k_2=5 10^{-8} according to equation 4.

5.3 Kinetics of evaporation

The numerical result of evaporation with degree of saturation and with time fit well with the experimental data except for the first period. The estimated evaporation rate of CRP coincided with the data. The high evaporation of the first period could not be reproduced due to the fact that the mass transfer coefficient between the surface and the ambient was obtained from the average evaporation rate in the CRP period. Therefore, it was not possible to get a coefficient value higher that during the CRP (Section 4.4). However, the CRP period lasted longer and there was overestimation of evaporation during FRP period (Figure 7). In order to deal with the problem, high evaporation rate was introduced to the pre-CRP period (i.e. saturated state Sr ~0.8), and then the prediction curve fit well the experimental data (R^2 > 0.9) (Figure 8).

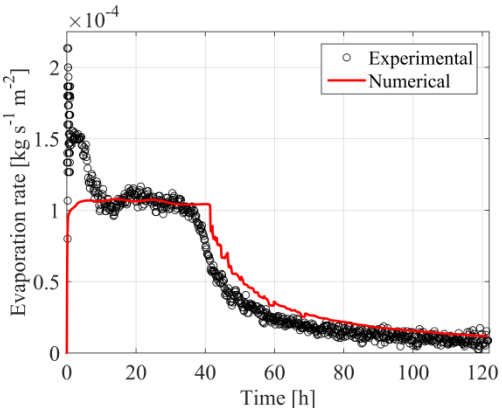

Fig. 7. Experimental and prediction of soil evaporation rate

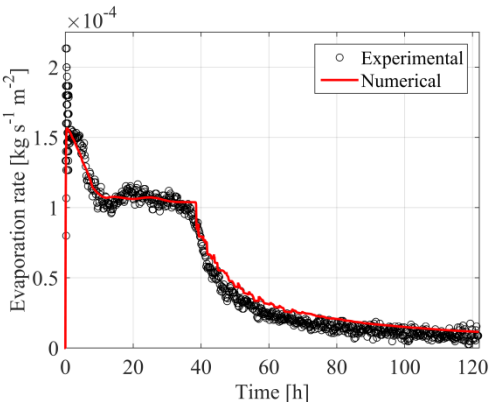

Fig. 8. Improved numerical prediction of soil evaporation rate

5.4 Soil temperature

The model managed somehow to predict the temperature variation during the experiment. Temperature started from 28°C to the plateau of 32°C which was the wet-bulb temperature (Figure 9). There was faster increase of the predicted temperature in the beginning. The reason was that the high evaporation rate during the pre-CRP was not predicted.

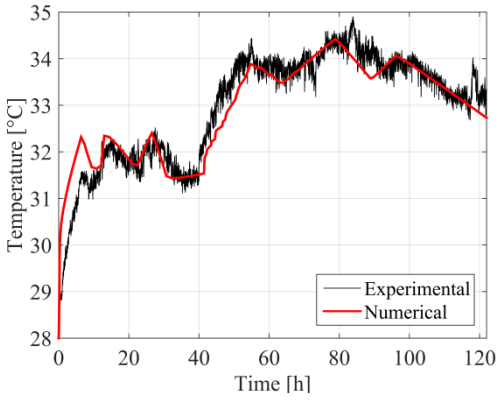

Fig. 9. Experimental and predicted soil surface temperature

5.5 Water transfer

The moisture transport during drying can be investigated based on Coussy [25] theory. It indicated that material

with permeability below 10-19 m^2 presented mainly Darcean advective water transport. Water was in liquid form and very negligible vapour diffusion. Therefore, the Luvisol was dominated by advective flow as its intrinsic permeability was of magnitude of 10-12m^2. Moreover, Figure 10 showed that moisture was mostly removed by Darcean advective flow. Figure 11 portrayed the humidity distribution in the sample. The entire sample has 100% humidity during saturation. There was formation of evaporation front (dry-and-wet front) when the soil start to de-saturate. The front moved to bottom as the soil kept on drying.

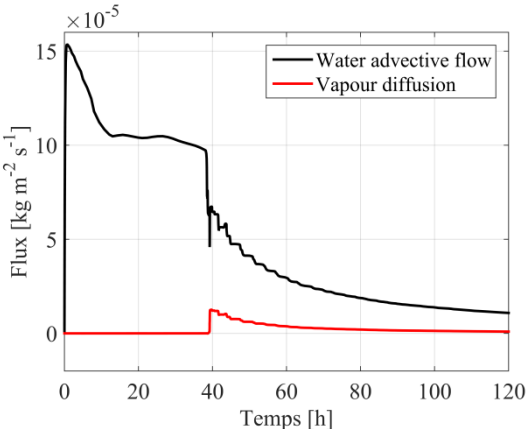

Fig. 10. Temporal evolution of water and vapour flow at the soil surface

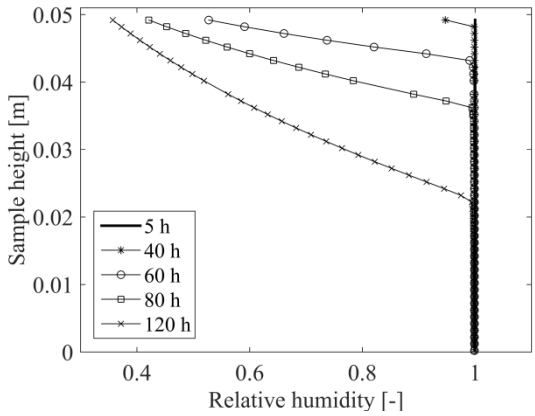

Fig. 11. Relative humidity profile along the sample with times

6. Conclusion

The study showed the process of evaporation of Luvisol in experimental and numerical approaches. Four evaporation periods were identified instead of three during the laboratory test. The temperature trend followed the Krischer's curve except that the current study recorded higher wet-bulb temperature due to higher radiation heat (>30°C). The fully coupled thermal-hydraulic-mechanical model managed to reproduce soil surface shrinkage, the temperature variation and the soil evaporation processes especially when correction was added during the start of evaporation. The moisture transfer mechanism of the agricultural Luvisol involved mainly Darcean advective flow. Vapour diffusion contributed a little during the entire process of evaporation. The evaporation front move from the soil surface to the bottom as the soil continued to dry. There is need for further research on another type of soil and on soil presenting cracks.

References

1. R. Core, A. Pachauri, A.E. Reisinger (tech. rep., IPCC, 2007)
2. A. Léonard, S. Blacher, P. Marchot, J.P. Pirard, M. Crine, Dry. Tech., **23**, 8 (2005)
3. R. Keey, M. Suzuki, Int. J. Heat. Mass. Tran. **17**, 12 (1974)
4. W. Coumans, Chem. Eng. Pro. **39**, 15 (2000)
5. X. Peng, R. Horn, Eur. J. Soil Sci. **58**, 9 (2007)
6. M. Kutílek, Dev. Soil Sci. **24**, 29 (1996)
7. J. Simunek, N. J. Jarvis, M. van Genuchten, A. Gärdenäs, J. Hydrol. **272**, 21 (2003)
8. S. Das Gupta, B. P. Mohanty, J. M. Köhne, Soil Sci. Soc. Am. J. **70**, 9 (2006)
9. Y. L. Bray, M. PratInt. J. Heat Mass Transf. **42**, 17 (1999)
10. M. Suzuki and S. Maeda, J. Chem. Eng. Jpn. **1**, 7 (1968)
11. M. Prat, Dry. Technol. **9**, 27 (1991)
12. P. Gerard, A. Léonard, J.-P. Masekanya, R. Charlier, and F. Collin, Int. J. Numer. Anal. Methods Geomech. **34**, 23 (2011)
13. N. Prime, Z. Housni, L. Fraikin, A. Léonard, R. Charlier, and S. Levasseur, Tran. Por. Med. **106**, 25 (2015)
14. N. An, S. Hemmati, Y. J. Cui, and C. S. Tang, Eng. Geol. **234**, 9 (2018)
15. J. Hubert, E. Plougonven, N. Prime, A. Léonard, and F. Collin, Int. J. Numer. Anal. Methods Geomech. **42**, 19 (2017)
16. F. Collin, X. Li, J. Radu, and R. Charlier, Eng. Geol. **64**, 14 (2002)
17. S. J. Kowalski, *Thermomechanics of Drying Processes* (Springer, Berlin, Heidelberg, 2003)
18. R. Stull, J. Appl. Meteorol. Clim. **50**, 2 (2011)
19. T.B. Edil, S.E. Motan, Trans. Res. Rec. **705**, 9 (1979)
20. D. Fredlund, A. Bergan, and P. Wong, Trans. Res. Rec. **8** (1977)
21. A. Sawangsuriya, T.B. Edil, P.J. Bosscher, J. Geotech. Geoenviron. **135**, 13 (2009)
22. W. Durner, Water Resour. Res. **30**, 12 (1994)
23. Y. Mualem, Water Resour. Res. **12**, 9 (1976)
24. S. Nasrallah, P. Perre, J. Heat Mass Transf. **31**, 10 (1988)
25. O. Coussy, *Poromechanics* (Wiley-Blackwell, 2005)